Daif Rahuna [1,2], I Ketut Aria Pria Utama [3,], Erwandi [2], Dendy Satrio [1]*

An investigation into the use of vortex generators on the blade of vertical axis current turbine in correlation with delaying stall and increasing energy efficiency

[1]Departement of Ocean Engineering, Institut Teknologi Sepuluh Nopember (ITS), Surabaya, Indonesia
[2]National Research and Innovation Agency (BRIN), Surabaya, Indonesia
[3]Departement of Naval Architecture, Institut Teknologi Sepuluh Nopember (ITS), Surabaya, Indonesia
*Corresponding author: kutama@its.ac.id

Original scientific paper
Received: December 15, 2025
Accepted: May 13, 2026
https://doi.org/10.65776/ep.21.1.1

This work is licensed under a Creative Commons Attribution 3.0 Unported License.

Abstract

The common phenomena in vertical-axis turbines arise from the continuously changing angle of attack (AoA), which results in; flow separation, dynamic stall, unsteady hydrodynamics, complex wake and vortex structures, and Cyclic structural loading. Devices such as vortex generators (VGs) are used to mitigate flow separation and dynamic stall, thereby significantly improving turbine performance. Numerical simulations investigate the effect of VG addition on turbine performance in general, specifically the NACA 0021 blades in the H-type Darrieus turbine. The single-blade model was equipped with rectangular VGs of specific dimensions, arranged in a single row and contra rotating. Computational Fluid Dynamics (CFD) simulation using ANSYS-FLUENT was employed as the numerical approach to compare the performance of an NACA 0021 blade with and without rectangular VGs. The VGs were placed at chordwise positions of 20%c, 25%C, and 30%c. The simulation results show that the most effective VG placement is at 25%c, where the drag coefficient is reduced by up to 38.0% at an AoA of 15°, and by 17.3% at AoA = 20°, compared to the clean airfoil without VGs. This study shows that the addition of VGs reduces drag and enhances turbine performance. The reduction in drag influences the flow separation behavior, thereby delaying stall.

***Keywords**: Vortex Generator, Drag Reduction, Stall Delay, airfoil NACA 0021, Vertical Axis Ocean Current Turbine (VACT)*

1. Introduction

Flow control approaches can be utilized to prevent boundary layer (BL) separation and stalling. Vortex generators (VGs) were originally proposed by Taylor in 1947 [1], to increase lift and decrease drag by delaying stall at an aircraft's wing, in aviation [2]. When VG is on the upper surface of the wing, it helps maintain airflow attachment to the wing at high angles of attack, reducing stall speed and/or making the control surfaces more effective. The Boeing 737 utilizes VG devices not only on the wings but also on the horizontal stabilizer and the forward fuselage. The addition of VGs serves to stabilize airflow over the vertical and horizontal stabilizers, help control airflow at high speeds, and reduce hydrodynamic noise that could disturb the pilot [3].

In the energy sector, VGs are the best choice to improve the performance of horizontal axis wind turbines (HAWTs), due to their good enhancement effect, low cost, and easy application [4]. VGs transfer momentum from the outside free-stream flow to the wall area, then increase the near-wall momentum, when the flow is separated from the blade surface in a smooth blade case [5]. The condition known as dynamic stall is a dynamic and unstable phenomenon. In addition, VGs can minimize vibration, noise, and fatigue stresses caused by stalls on the blades, to improve performance and energy production, thus attracting much research interest [6][7].

In general, vertical axis current turbines (VACTs) have disadvantages, especially in low turbine performance efficiency, poor self-starting, cavitation, and vibration [8] [9]. However, VACTs have advantages including, accepting flow from all directions, easy maintenance, low cost and simple construction. Therefore, this has driven researchers to develop VACT. Many studies have developed VACT, aiming to improve turbine performance in recent decades.

Extensive research has been conducted to improve the self-starting capability of VACTs, including modifications to turbine geometry and flow control approaches. The geometric modifications involve variable pitch control [10][11], inclined blades [12], changes in blade angle [13], the addition of auxiliary rotors [14], the use of winglets [15][16][17], and helical blades [18]. Meanwhile, augmentation devices are used to alter the fluid flow behaviour around VACTs, such as flow disruption [19] [20], flow deflectors [21], tubercles [22][23], and VGs, which are the focus of this study.

Several recent VG studies have been developed to gain more details on the flow mechanism and the best VG shape design methodology to produce optimal VG performance on aerofoil types. The best VG design is often based on vortex peaks, vorticity trajectories, dimensions, and steady flow velocity. Dimensions, placement location and configuration play an important role in accelerating vortex formation, thereby improving aerofoil performance [24][25]. These studies suggest that no single VG model has proven superior

to others in representing the impact of VGs on flow using body forces [5][26]. Mueller-Vahl et al. observed that a small VG distance not only resulted in a stall delay of up to 12.5° from the stall AoA, and a 31% increase in the maximum lift coefficient ($C_{l,max}$.), but also reduced the drag coefficient. Reducing the distance causes increased interaction of the surrounding vortices so that the vortices move further from the airfoil surface [27]. A study on the DU97-W-300 airfoil with added VGs showed that the chordwise position of the VGs and the blade height were the most important factors for airfoil performance, but blade length, pitch angle, blade shape, and stacking density proved to be secondary factors [28]. In another study, the influence of rectangular VGs arranged in a dual-row configuration on the flow around the NREL S809 airfoil was investigated through numerical simulation. The findings revealed that the second row of VGs contributed to a greater suppression of flow separation, leading to a $C_{l,max}$.. increase of 0.27 compared to the single-row configuration positioned near the leading edge [29]. The study conducted by Binbin Wei et al. investigated the use of VGs as a passive flow control method to reduce dynamic stall on wind turbine and helicopter rotor airfoils. Using a NACA 0012 airfoil and wind tunnel experiments, the study showed that VG installation could delay flow separation, reduce dynamic stall vortices, and improve aerodynamic stability at high angles of attack. The research also found that the position and configuration of the VG greatly affect its effectiveness in improving aerodynamic performance [30].

The purpose of this study is to explore the stall delay, lift force and drag force to maximize turbine performance by obtaining the highest lift and lowest drag and to assess the flow pattern affected by the addition of VG. The profile used as a benchmark is NACA 0021, a 21% thick airfoil with a chord of 0.14 m and a span of 0.28 m, at a Reynolds number of 1.917×10^5. Furthermore, we add VG to the surface of both rectangular profiles, adjusting their placement and dimensions accordingly. The approach uses numerical simulation to analyze the effect of VG on the NACA 0021 airfoil of VACT with the Reynolds-averaged Navier-Stokes (RANS), based Computational Fluid Dynamics (CFD) approach using the k-ω SST (shear stress transport) of turbulence model.

1.1 State of the art

This study differs from previous research by placing the VG below the hydrofoil profile in the CFD analysis. The investigation covers an angle of attack range from 0° to 45° in the turbine rotation direction, whereas previous studies commonly installed VGs on the upper profile. It is like the aeroplane wings concept.

The main difference of this study compared to previous ones is associated with the designation of the positive azimuthal angle (θ^+). While rotating from $\theta = 0°$, the azimuthal angle is designated as positive (θ^+), while the projected angle of attack is named as the positive angle of attack (α^+). If blade rotation is happening towards $\theta = 0°$, the azimuthal angle is named negative (θ^-), while the projected angle of attack is called the negative angle of attack (α^-). Much research has been done with profiles incorporating VG at moderate negative angles of attack, whereas there is very little data for positive angles of attack.

This arrangement is especially crucial since the turbine blade meets the incoming stream at the highest velocity relative to each other in this case. Therefore, the blade experiences the greatest hydrodynamic force that is necessary for creating rotation, which improves the efficiency of the turbine.

2. Methodology

In this paper, the numerical simulation approach used is on a single blade, where a single blade is a blade that does not cover the entire turbine, while in general, the turbine consists of several blades (more than one). The model used in the numerical simulation includes the original blade in the form of a symmetrical NACA-0021 foil without and with the addition of VGs, where the VG is rectangular with differences in placement on the foil surface. The purpose of this numerical simulation is to provide initial insight into the effects of adding VGs to the blades compared to no VGs, as well as the effects of VG shape and placement on stall delay, lift coefficient (C_l), and drag coefficient (C_d).

This section explains the flowchart that clearly and concisely outlines the step-by-step process of the research, serving as a focused framework for evaluating the effectiveness of adding VGs to improve the performance of the NACA 0021 foil used as a blade in a VACT system. The main procedural steps are illustrated in **Fig. 1**. The initial step involves defining the geometry and preparing the computational domain, which is described in detail. The next steps include mesh generation, a grid independence study, boundary condition configuration, and solver setup. The validation process involves evaluating solver settings and remeshing if the results deviate from the expected validation trends. The implementation of rectangular VGs in the simulation will proceed only once the validation criteria are met. The results section presents findings for three key parameters: C_l and C_d. It also includes contour analysis of the flow behavior around the blade, both with and without VGs. The final part of the study provides a performance prediction of VG implementation on VACT, specifically assessing the application of VGs on the NACA 0021 foil within a VACT configuration.

2.1 CFD Modelling

The computational domain was developed using ANSYS Design Modeler, with mesh generation conducted in ANSYS Meshing. To ensure fully developed flow and minimize boundary-induced effects, the domain was sized at 30*c*, consistent with best practices established in prior hydrodynamic studies [6]. The domain configuration is optimized to facilitate AoA (α) parameterization through the manipulation of inlet velocity components, thereby enabling the simulation of varying α without altering the hydrofoil's geometric orientation or creating multiple model instances [31].

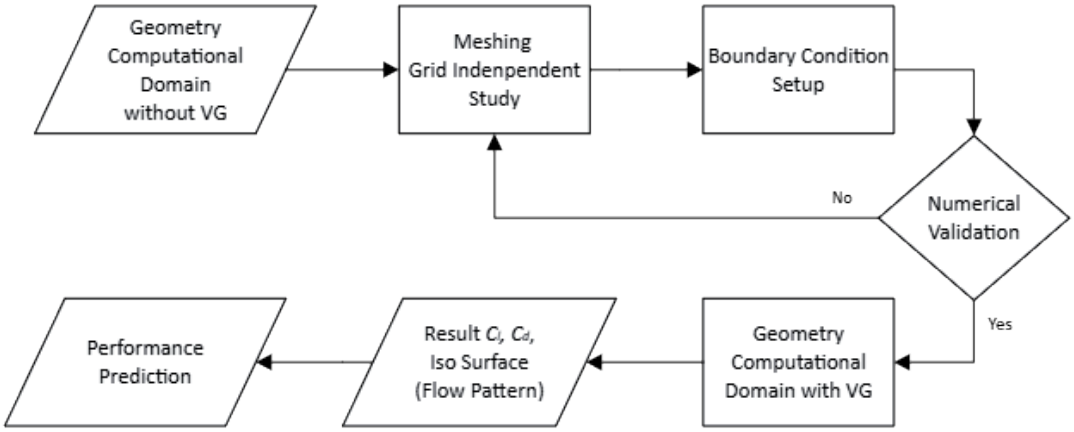


Fig. 1. CFD methodology

The computational domain is cylindrical with the hydrofoil located at the center of the cylinder. The diameter of the domain is 30c to ensure that the fluid flow is fully developed [32]. It is easier to implement the inlet α parameterization. By changing the inlet velocity components to simulate different α, there is no need to create another model with varying orientations of hydrofoil [25]. The simulations are performed in the α range of 0°-45° with an increment of 5°. However, it is important to note that the angle between 0°-40° is considered as the critical α, so the analysis is focused on the hydrofoil performance. Therefore, the increment is increased to 2° in the range to produce a smoother curve shape and capture the phenomenon in detail [25].

The domain geometry is generated using ANSYS Design Modeler. A hybrid O-topology grid is employed for the clean profile, with the domain's radius set to 15 of the chord lengths. A hybrid O-topology grid is employed for the clean profile, with the domain's radius set to 15 of the chord lengths. The boundary conditions used during the numerical simulation, which were adjusted to match the test conditions conducted by holst, 2019. The test conditions used air as the working fluid, on a Reynolds number (*Re.*) of 1.917×10^5, a velocity of inlet 20 m/s, a turbulence intensity of 1%, and a viscosity ratio of 6 [6]. Boundary conditions in the numerical simulation are adjusted to test conditions. Side boundaries were set as symmetry to replicate the extended range used in further research. Hydrofoil surface and VG were set as no-slip wall boundary conditions. The low Reynolds number indicates that the hydrofoil may have difficulty in self-starting due to the lower fluid velocity.

2.2 Geometry Modeling

This modeling strategy enhances computational efficiency while ensuring consistent boundary conditions across all cases. It further allows for a continuous sweep of α values, typically ranging from 0° to 180°, which is essential for accurately capturing the hydrodynamic response of the hydrofoil, particularly in the critical stall region. Such an approach is highly advantageous for evaluating unsteady flow phenomena and performance degradation due to flow separation.

The numerical approach is done with a turbine model with and without VG addition. The shape of the VG rectangle, with VG placement location, varies between 10%-30% of chord length (c) with 5% interval, and single row contra-rotating configuration The dimensions of the VG and the shape of the VG consisting of a rectangle are shown in **Table 1**. The dimensions of VGs based on data obtained from researchers who have conducted previous research include height, h, (h/c), length, p, (l/h), angle (β), the distance between VG (p/h), front distance (f/h), and rear distance (r/h), as represented in **Fig. 2**.

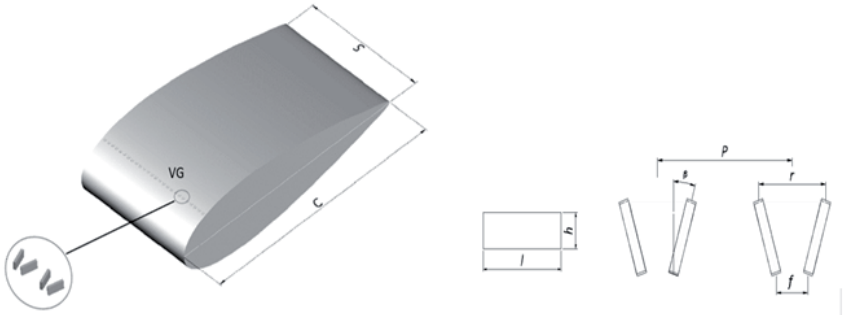


Fig. 2. VGs Schematic on the blade.

Table 1. Turbine and VG specifications for numerical simulation.

Part	Name/parameter	Specification/value
VACT Blade	*Hydrofoil type*	NACA 0021
	Number of blade (N)	3
	Chord length (c)	0.14 m
	Span (S)	0.28 m
	Sudut pitch	0^{O}
	Angle of attack, AoA (α)	$0 – 45^{o}$
Vortex generator	*VG Shape*	rectangular
	Location Position	20%c, 25%c, 30%c
	Configuration	single-row, contra-rotating
	Height (h/c)	Small VG parameters, as seen in Table 2
	Length (l/h)	3
	Angle (β)	18^{o}
	Pair distance (p/h)	7
	Rear distance (r/h)	3.5
	Front distance (f/h)	1.65

In the numerical simulation of a foil with the addition of VGs, several variations are considered, including the dimensions and placement of the VGs, as shown in **Table 2**. The height of the VG changes for each difference in VG position relative to the chord length. This is because the VG height equals the boundary layer (BL) thickness at each placement location on the foil surface [33]. The relative height of VGs is typically represented by the variable h/δ, where h denotes the VG height and δ represents the boundary layer thickness. Based on their height, VGs are categorized into two types: conventional VGs ($h/\delta \geq 1$) and submerged VGs ($0.1 < h/\delta < 0.5$), also known as "micro" or "low-profile" VGs [34]. Every change in VG height always affects other VG dimensions, such as length (l), spacing between VG pairs (p), and the total number of VGs along the span for each variation of placement location (x/c).

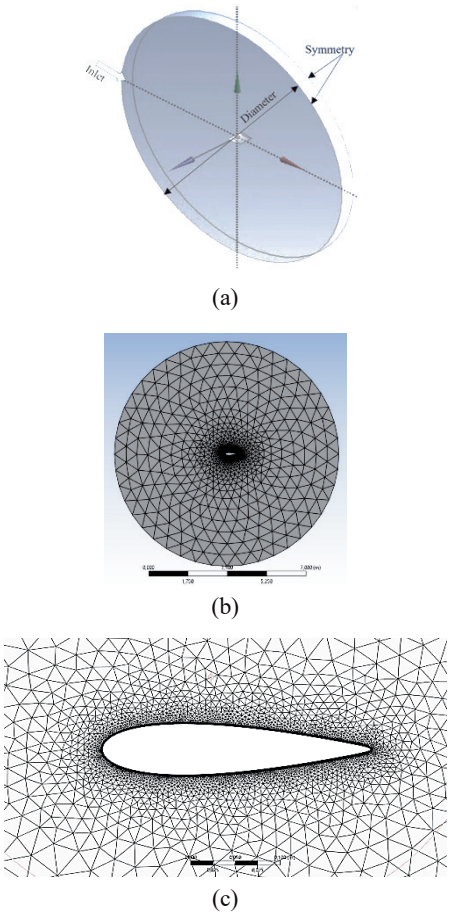
Table 2. Main parameters of the small VGs simulated in this study.

x/c	*h (mm)*	*l (mm)*	*p (mm)*	*r (mm)*	*f (mm)*
20%	0.60	1.80	4.20	2.10	0.99
25%	0.72	2.16	5.04	2.52	1.19
30%	0.87	2.61	6.09	3.05	1.44

2.3 Validation

The grid was generated using ANSYS Meshing software. The mesh comprises three distinct regions: a structured, multi-block section in the boundary layer, an unstructured region surrounding the airfoil to maintain an approximately constant cell size, and another structured region encompassing the outer domain. For the clean profile configuration, a hybrid O-type topology is employed with a domain radius of 15c to minimize far-field boundary effects. The mesh consists of three zones: a structured multi-block region for accurate boundary layer resolution, an unstructured region around the hydrofoil for flexibility and uniform cell distribution, and an outer structured region extending to the far field to improve numerical stability and overall grid quality.The computational domain is defined as a circular region with a diameter sufficiently large to minimize boundary interference effects on the flow around the hydrofoil, as represented in **Fig.3a**. A velocity inlet boundary condition is applied at the upstream region to prescribe a uniform incoming flow. The downstream boundary is treated as an outlet, allowing the flow to exit the domain without reflection.

The lateral boundaries are defined as symmetry conditions, which imply zero normal velocity and zero normal gradients for all flow variables. This assumption reduces computational cost while maintaining physical accuracy for external hydrodynamic flow. The profile surface itself is modeled as a no-slip wall, enforcing zero velocity at the surface to capture boundary layer development.



(a)

(b)

(c)

Fig. 3. Computational mesh for clean foil NACA 0021

In this study, the mesh for the original NACA 0021 foil consists of 1,467,950 elements and 407,450 nodes. The finest mesh resolution is concentrated around the foil, with a growth rate of 1.2. The overall mesh distribution within the computational domain is illustrated in **Fig. 3b**, while the refined mesh structure surrounding the foil is also depicted **Fig. 3c**. An inflation layer technique is employed along the foil surface to accurately capture the boundary layer effects, with the first layer thickness set to 0.00007636 m.

A target y^+ value of 0.85 is used to ensure adequate near-wall resolution and improve boundary layer accuracy. Keeping $y^+<1$ allows proper resolution of the viscous sublayer, consistent with the requirements of the *k–ω SST* turbulence model, and enables wall-resolved simulations without wall functions. This improves the prediction of shear stress and pressure distribution along the hydrofoil surface.

Table 3. Mesh Quality

Quality	Foil NACA-0021
skewness	0.2168
orthogonal quality	0.7813
aspect ratio	5.7708

To achieve this, the mesh near the wall is refined using a first inflation layer height of 1.298x10-5m, with 9 inflation layers and a growth rate of 1.2. This configuration ensures accurate capture of boundary layer development, separation, and reattachment, which is essential for evaluating the hydrodynamic performance of the hydrofoil with micro-VGs.

As summarized in **Table 3**, the generated mesh demonstrates satisfactory quality. The skewness values remain below 0.25, indicating well-shaped elements with minimal distortion. The orthogonal quality is consistently above acceptable thresholds (approaching unity), reflecting good alignment between cell faces and flow gradients. Additionally, the aspect ratio ranges between 0.5 and 0.8, suggesting balanced element proportions without excessive stretching.

Secondly, a mesh was generated for the NACA 0021 airfoil model incorporating VGs, with the height of each VG matched to the local boundary layer thickness, as shown **Fig. 4**. This thickness varies along the chordwise position (x/c), being thinner near the leading edge and gradually increasing toward the trailing edge, as detailed in **Table 1**. To ensure consistency, the same meshing strategy applied to the original airfoil was also used for the airfoil equipped with VGs.

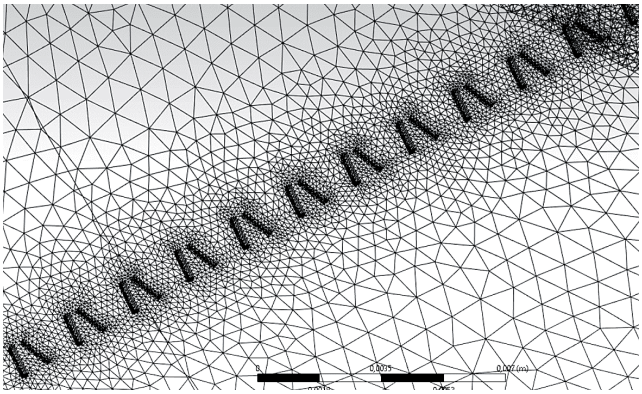


Fig. 4. Mesh generation for the foil with integrated VGs

A mesh independence study was carried out on the hydrofoil model without VG at an α of 10°. The resulting C_l and C_d from the simulation were validated against the experimental data of [6]. A grid independence test was performed using the coupled second-order upwind method to evaluate the grid independence (GI) values for C_l and C_d across varying element counts: The 365,782-element mesh is now explicitly described in the grid independence section as a preliminary mesh sensitivity check. This mesh level was initially employed to obtain a first-order assessment of solution behavior and to identify a suitable range for subsequent systematic refinement. The formal convergence study, therefore, focuses on the three progressively refined meshes—coarse (733,522 elements), medium (1,467,736 elements), and fine (2,935,503 elements), as these satisfy the requirements for consistent refinement ratio and reliable estimation of numerical uncertainty. The findings of this study elucidate the influence of element count variations on the measured values

of C_l and C_d. As shown in **Table 4**, The grid independence test (GIT) conducted between the medium and fine grids yielded results of 0.019 for C_d and 0.043 for C_l.

Table 4. Verification outcomes were obtained through the application of the GI method.

Elements Number	C_d	*GI*	C_l	*GI*
365,782	0.0356408	-	0.5978161	-
733,522	0.0351602	0.032	0.6026012	0.022
1,467,736	0.0354005	0.019	0.6118848	0.043
2,935,503	0.0356692	0.060	0.6145331	0.013

The order of convergence (p) estimates how fast the numerical solution improves with grid refinement. It is computed from solutions at successive grid levels and indicates how effectively discretization error is reduced. A p value close to the method's formal accuracy shows consistent convergence, while deviations may indicate nonlinear effects or remaining numerical errors.

$$p = \frac{\ln\left|\frac{\varepsilon_{32}}{\varepsilon_{21}}\right|}{\ln(r)} \quad (1)$$

Richardson extrapolation is used to estimate the solution on an infinitely fine grid:

$$\phi_{ext} = \phi_1 + \frac{\phi_1 - \phi_2}{r^p - 1} \quad (2)$$

The GCI is calculated using the difference between solutions on refined grids, the grid refinement ratio, and the estimated order of convergence. A safety factor (Fs) is applied to provide a conservative estimate of numerical uncertainty, which is expressed as a percentage and used to assess the sensitivity of the solution to grid resolution. Fs = 1.25 is the safety factor recommended by Roache. A small GCI value indicates weak dependence of the numerical solution on grid resolution, whereas a large GCI value reflects significant sensitivity to grid refinement and non-negligible discretization errors. Formula of the GCI:

For the medium $_2$ - coarse $_1$ grid pair:

$$GCI_{21} = F_s \frac{|\phi_1 - \phi_2|}{|\phi_1|(r^p - 1)} \times 100\% \quad (3)$$

For the fine $_3$ - medium $_2$ grid pair:

$$GCI_{32} = F_s \frac{|\phi_2 - \phi_3|}{|\phi_2|(r^p - 1)} \times 100\% \quad (4)$$

Table 5. Verification outcomes were obtained through the application of the GCI method.

Elements Number	C_d	*GCI*	C_l	*GCI*
365,782*	0.03564		0.59781	
733,522	0.03516	0.013	0.60260	0.011
1,467,736	0.03540	0.009	0.61188	0.011
2,935,503	0.03566		0.61453	

** preliminary mesh sensitivity check*

Verification of the asymptotic range confirms that the solution converges consistently with grid refinement. The GCI and refinement ratio indicate the solution lies within this range, so the associated numerical uncertainty is considered valid.

$$\frac{GCI_{32}}{GCI_{21}} \approx r^p \quad (5)$$

In addition to the GI, it is also essential to assess the error ratio between two different grid resolutions, as the Grid Convergence Index (GCI) method serves as a valuable tool for understanding how errors decrease with increasing grid resolution. As shown in **Table 5**, In this verification process, numerical uncertainty is quantified using GCI method, which is based on the Generalized Richardson Extrapolation [35].

3. Result and Discussion

3.1 Lift and Drag Coefficients

The numerical simulation results were compared with experimental data using scale-resolving methods. **Fig. 5** illustrates the relationship between the lift coefficient and the variation of angle of attack (AoA), ranging from 0° to 45°, with 5° intervals. The numerical simulations were conducted for a NACA 0021 airfoil equipped with rectangular VGs, arranged in a single row at various chordwise positions (20%c, 25%c, and 30%c). The height of each VG (h) was matched to the local boundary layer thickness (δ) at each corresponding placement position. The simulation results indicate that the addition of VGs leads to an increase in lift coefficient compared to the baseline configuration without VGs, particularly at α = 15°. The most significant lift enhancement occurred at the 30%c position, where the peak lift coefficient reached 6.7%, followed by the 20%c position with a peak lift coefficient of 5.7%, and the 25%c position with 2.0%, all relative to the airfoil without VGs. At an angle of attack of 20°, the greatest increase in lift coefficient 7.4% was achieved with the VGs positioned at 25% chord. Positioning them at 30%c yielded a 5.4% increase in lift coefficient, while placement at 20%c produced a 3.7% increase.

The implementation of VGs on the airfoil led to a considerable reduction in the drag coefficient. The most signifi-

cant reduction was recorded at the 25%c location, reaching 38.0%, followed by reductions at the 30%c and 20%c positions, which achieved 37.4% and 27.3%, respectively, in comparison to the baseline configuration without VGs, as shown in **Fig. 6**. At α = 20°, the highest drag reduction was again recorded with the VG positioned at 25%c, achieving a 17.3% decrease in drag coefficient. This was followed by reductions of 10.3% and 8.3% for VG placements at 20% and 30% chord, respectively. The simulation outcomes demonstrate that positioning the VG at 25%c on the symmetric NACA 0021 airfoil yields a marked decrease in drag coefficient, accompanied by a significant improvement in lift performance, thereby contributing to stall delay.

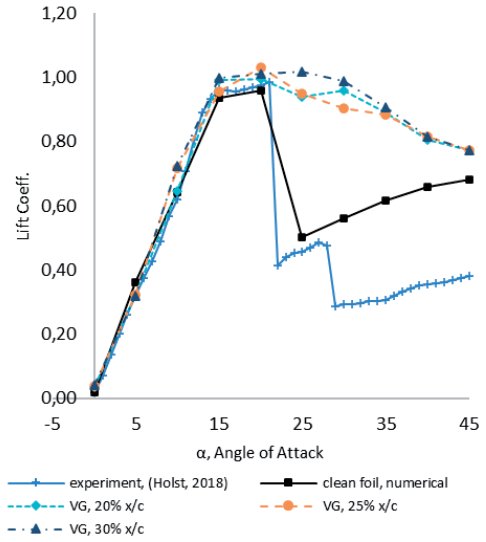


Fig. 5. Lift Coefficient of the NACA 0021 foil

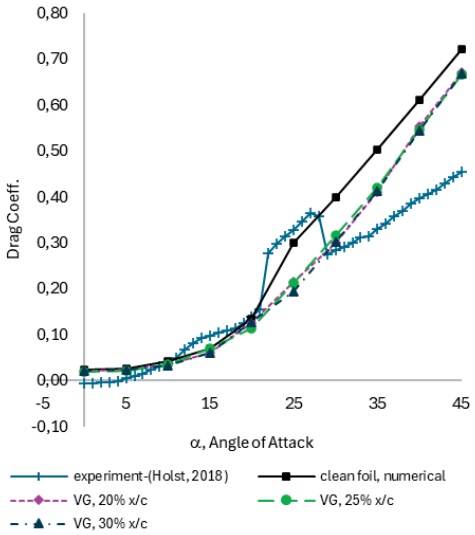


Fig. 6. Drag Coefficient of the NACA 0021 foil

3.2 The lift-to-drag (C_L/C_D) ratio

The C_L/C_D ratio is basically used to understand the shape when interacting with fluid. The coefficient of the C_L/C_D ratio significantly influences the energy efficiency of wind turbines by determining the optimal power coefficient. A higher C_L/C_D ratio allows for better hydrodynamic performance, leading to increased power output. C_L represents how much useful force is generated, like the upward force on a wing or the driving force on a turbine blade. Meanwhile, C_D represents the resistance that tries to slow everything down.

The C_L/C_D ratio tells us how efficiently a shape converts fluid flow into useful force compared to how much energy is lost to drag. A high C_L/C_D ratio means the design generates a lot of lift with little drag. This is what engineers prefer, as it means better performance and less wasted energy. On the other hand, a low ratio means the profile performs poorly.

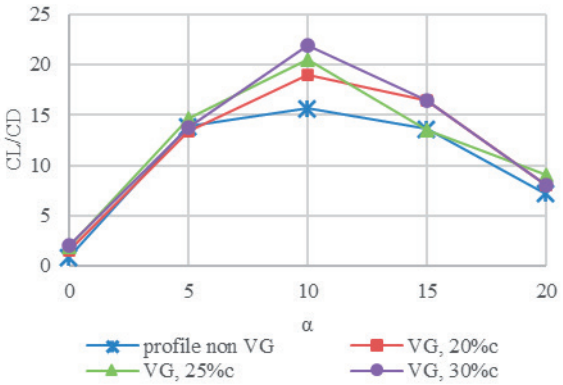


Fig. 7. Ratio C_L/C_D

This **Fig. 7** compares the hydrodynamic efficiency (C_L/C_D) of a standard wing profile against those equipped with VGs at various angles of attack (α). Overall, the addition of VGs consistently enhances the wing's performance across all angles, with peak efficiency for every configuration occurring at a 10°. Among the tested variations, placing the VG at the 30% position yields the most optimal results, achieving the highest lift-to-drag ratio compared to the baseline profile and other VG placements.

The C_L/C_D ratio improves when VGs are added to the original profile. The most noticeable improvement occurs when the VGs are placed at 30%c, resulting in a 21.4% increase. When positioned at 25%c, the ratio increases by 16.5%, while placement at 20%c leads to a 14.2% improvement. Overall, these results show that the position of the VGs plays an important role in enhancing hydrodynamic efficiency, with the 30%c position giving the best performance among the cases studied.

3.3 Velocity field

Fig. 8 illustrates the velocity magnitude contours around the airfoil for angles of attack ranging from α = 0° to 45°, comparing the profile with and without VG. The contour levels represent the local flow velocity, where low-velocity regions (blue) indicate flow deceleration and potential separation, while higher velocities (green to yellow) correspond to accelerated flow regions.

At low angles of attack ($\alpha \leq 10°$), the flow remains predominantly attached over the airfoil surface for both configurations. The velocity distribution is nearly identical, indicating that the inclusion of VG does not significantly

influence the flow field in the pre-separation regime. This is expected, as the boundary layer retains sufficient momentum to resist adverse pressure gradients.

As the angle of attack increases to moderate values ($15° \leq \alpha \leq 25°$), the onset of flow separation becomes evident in the baseline configuration. This is characterized by the emergence and downstream growth of a low-velocity region on the suction side. In contrast, the VG-equipped airfoil exhibits a noticeably reduced separated region. The presence of VG enhances momentum exchange within the boundary layer, thereby delaying separation and maintaining a more attached flow.

At higher angles of attack ($\alpha \geq 30°$), the disparity between the two configurations becomes substantial. The baseline airfoil develops a large separated flow region accompanied by an extensive low-velocity wake, indicating significant flow detachment and degraded aerodynamic performance. Conversely, the VG configuration demonstrates a more confined separation zone and a comparatively narrower wake. Although separation is not entirely suppressed, its spatial extent and intensity are clearly mitigated.

Overall, the results confirm that VGs are effective in delaying flow separation and reducing wake development under high-angle-of-attack conditions. This flow control mechanism contributes to improved aerodynamic characteristics, particularly in sustaining lift and limiting drag increase in the near-stall and post-stall regimes.

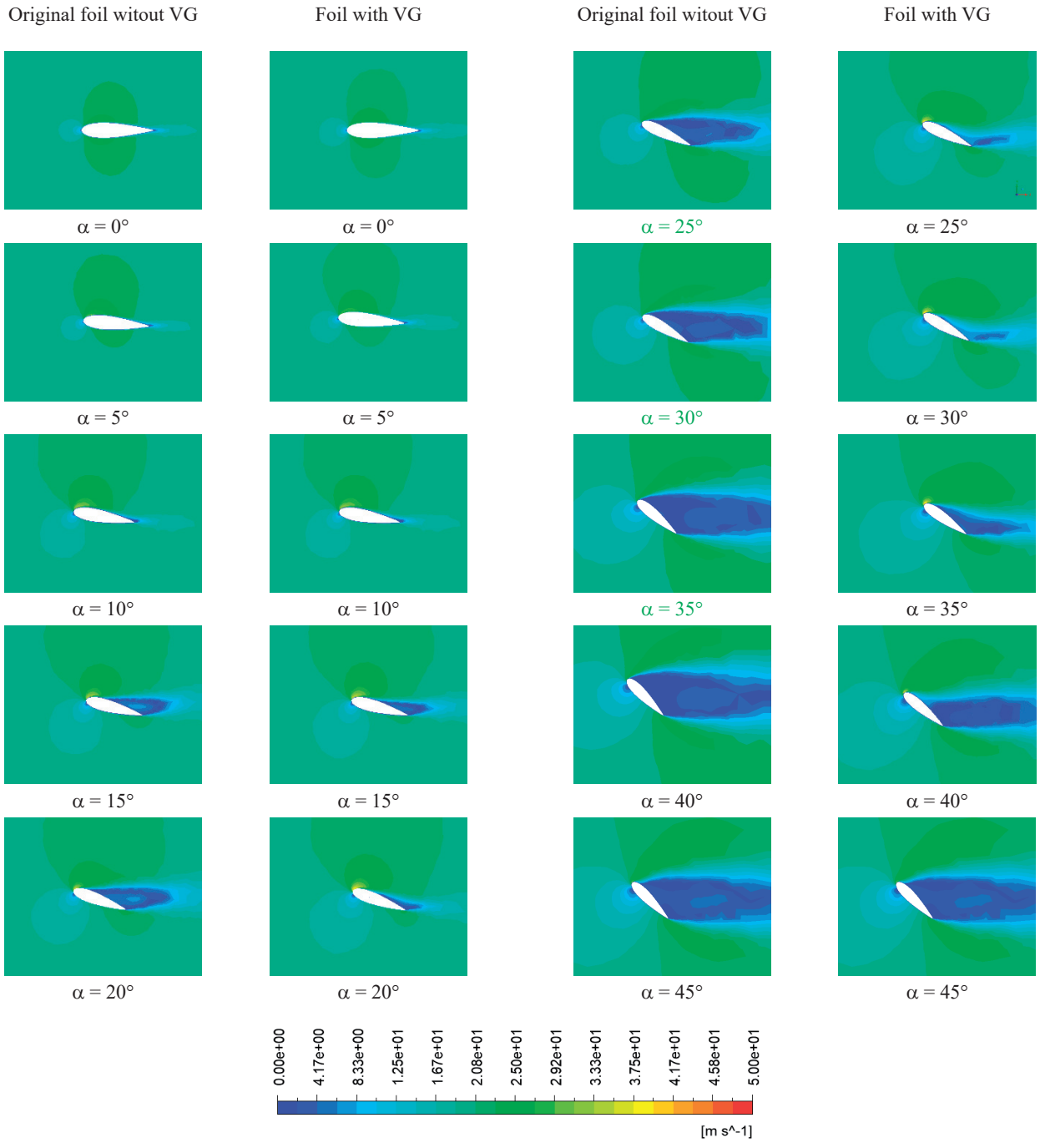


Fig. 8. Velocity magnitude at different AoA for both, profile without and with VGs at 25%c.

At higher angles of attack ($\alpha \geq 30°$), the baseline airfoil experiences extensive flow detachment, resulting in a large wake region and significant aerodynamic degradation. This is typically associated with a sharp decline in C_L/C_D. Conversely, the VG-equipped airfoil maintains a relatively more attached flow, with a smaller separation region and a more confined wake. This explains the ability of the VG configurations to sustain higher C_L/C_D values even in near-stall and post-stall conditions.

Overall, the contour visualization provides clear physical insight into the aerodynamic performance trends. The reduction in separation and wake size induced by VG leads to improved flow attachment, which directly translates into higher C_L/C_D. Therefore, the observed performance gains are not only quantitative but also strongly supported by the underlying flow physics.

When intermediate angles of attack ($15° \leq \alpha \leq 25°$) are reached, the airfoil not using VG starts developing flow separation on the intake side, which can be seen from the emergence of a low-speed zone. On the other hand, the VG case demonstrates separation delay along with a smaller size. This effect is tightly related to the rise of C_L/C_D ratio values, since it is evident that the case with VG provides an increment in C_L/C_D equal to about 14.2% (20%c), 16.5% (25%c), and 21.4% (30%c) relative to the case without VG.

For a steady, incompressible, and frictionless flow along a streamline, Bernoulli's principle holds that the sum of the fluid's static pressure, its velocity-dependent (dynamic) pressure, and its elevation (hydrostatic) pressure remains invariant:

$$p+0.5\,\rho v^2+\rho gh=constant \qquad (6)$$

In this expression, p represents the static pressure, ρ the density, v the flow speed, g the acceleration due to gravity, and h the height above a chosen reference. Thus, regions of higher flow velocity correspond to lower static pressure (and vice versa), reflecting the fluid's mechanical energy conservation.

Along an airfoil, the flow speeds up over the curved upper surface and slows down along the lower surface. By Bernoulli's principle, wherever the fluid velocity, v increases, the static pressure, p decrease so that constant along a given streamline. If it compares two streamlines-one just above the airfoil (speed, v_{top}) and one just below (speed, v_{bottom}). Since $v_{top}>v_{bottom}$, the pressure on the upper surface is lower than that on the lower surface. This net pressure difference integrated over the foil's planform produces lift, which is the fundamental mechanism by which an airfoil generates the force. This result underpins devices and phenomena such as airfoil lift.

This is attributed to the vortices generated by the VGs, which follow a curved or helical trajectory downstream along the surface while transporting high-energy fluid from the free stream into the near-wall region. This momentum exchange helps delay separation by energizing the boundary layer. However, as the vortex convects downstream, it gradually decays due to viscous diffusion and interaction with surrounding flow structures. The rate of decay depends on factors such as the VG geometry, Reynolds number, and boundary layer characteristics [36]. A well-designed VG ensures that the vortex remains coherent over a sufficient length to maintain flow attachment in critical regions of the airfoil.

3.4 VG integration increases turbine power with a theoretical approach.

The integration of VGs into a (VACT) based on simulation data and simplified calculations requires several assumptions. This approach is intended solely to obtain a preliminary prediction of the impact of VG integration on the VACT's performance. In general, achieving more accurate predictions requires further simulations involving the entire rotating turbine to comprehensively explore its overall behavior.

Fig. 9 shows the change in a single blade's speed vector over a single rotation. Even with constant rotating speed and wind speed, the resultant velocity and AoA vary in both direction and amplitude with azimuth angle. The upstream half-cycle ($0° < \theta < 180°$) of the bar is positive, whereas the downstream half-cycle ($180° < \theta < 360°$) is negative.

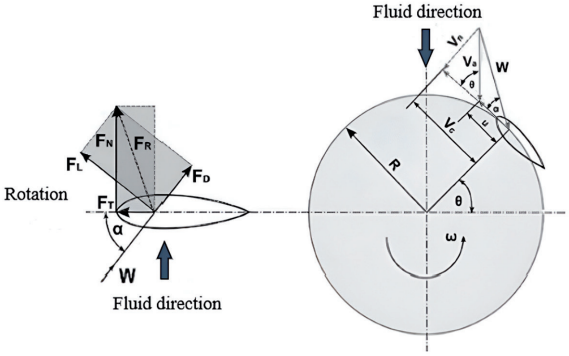


Fig. 9. Force and velocity vectors of a VAT [39]

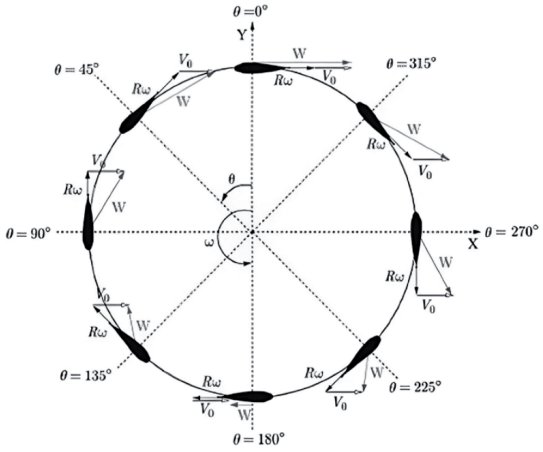


Fig. 10. Velocity vectors at different azimuth angles [43]

The hydrodynamic performance of vertical-axis turbines is characterized by complex flow phenomena, including

cyclic variations in the angle of attack, dynamic stall effects, and strong flow interference between the upwind and downwind passes of the blades (**Fig. 10**). To address these challenges and to provide a computationally efficient predictive tool, Paraschivoiu, (2002) developed the Double-Multiple Stream Tube (DMST) theory, an extension of the classical momentum and blade element theories, specifically tailored for Darrieus-type vertical axis turbines [37].

The fundamental principle of the DMST model is based on dividing the turbine's swept area into several independent stream tubes, each representing a discrete section of the flow field. Within each stream tube, the conservation of momentum is applied separately to the upwind and downwind regions of the turbine, hence the term double stream tube. This dual treatment allows for distinct induced velocity distributions in both regions, reflecting the fact that the downstream flow has already been influenced by the energy extraction occurring in the upwind half.

Each stream tube is analyzed independently, and the interaction between the hydrodynamic forces generated by the blades and the local flow conditions is evaluated using a blade element approach. The local induced velocities are iteratively updated until the momentum balance between the air stream and the blade forces is satisfied. Through this iterative process, the model predicts the distribution of hydrodynamic loads, torque, and power coefficients across the turbine's azimuthal positions.

The logical flow of the analysis is as follows: L and D forces are first transformed into normal (C_N) and tangential (C_T) force components, which are then used to compute the elemental torque (Q). The elemental torque is integrated to obtain the total rotor torque (Q_{total}), from which the mechanical power (P) and the power coefficient (C_p) are subsequently determined.

$$C_N = C_L \cos\alpha + C_D \sin\alpha \tag{7}$$

$$C_T = C_L \sin\alpha - C_D \cos\alpha \tag{8}$$

The relative inflow velocity (W) results from the vector combination of the local velocity (V) and the blade's tangential velocity due to rotor rotation ($R\omega$). Because the blade's direction of motion changes with azimuthal position, the magnitude of W varies over one revolution and directly governs the angle of attack (α) and the resulting aerodynamic forces on the blade.

$$\vec{W} = \vec{V} + \overrightarrow{R\omega} \tag{9}$$

The elemental torque (Q) generated by a blade element at a radial position (r) is obtained from the product of the elemental thrust force and the moment arm. By substituting the expression for the thrust force, the elemental torque can be written accordingly.

$$dQ(\theta) = r\,\frac{1}{2}\rho W^2(\theta)\,c\,\frac{C_T(\theta)}{\cos\delta(\theta)}\,dz \tag{10}$$

Since W, C_T, and δ are functions of the blade azimuthal angle (θ), the torque produced by the blade varies over one full revolution of the rotor.

The total torque generated by a single blade is obtained by integrating the elemental torque along the blade height. Subsequently, to determine the average torque over one full revolution, an integration is performed with respect to the blade's azimuth angle from 0 to 2π. For a rotor with blades number (N_b), the total torque (Q_{total}) is expressed as the summation of contributions from all blades

$$Q_{\text{total}} = N_b\,\bar{Q} \tag{11}$$

Mechanical power (P_m) produced by the rotor is subsequently determined by the product of total torque and angular velocity (ω):

$$P_m = Q_{\text{total}}\,\omega \tag{12}$$

Maximum kinetic power of the fluid (P) is:

$$P = \frac{1}{2}\rho A V_\infty^3 \tag{13}$$

VACTs type-H usually uses a symmetrical profile as a turbine blade part because of its ability to maintain lift performance on both sides of the blade when the turbine rotates. NACA 0021 is a symmetrical blade profile with a maximum thickness of 21% chord at 30% chord from the leading edge. This profile also has a peak C_l value of 0.98 [6]. In this study, VGs are applied to foils to investigate their functional effects between foils without and with VGs. The applied VGs are rectangular single-row VG arrays and counter-rotating configurations.

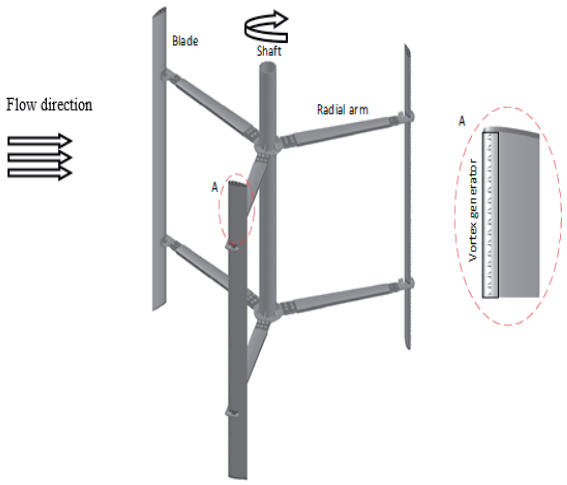


Fig. 11. Vertical axis current ocean turbine, H-darrieus type with VGs

Meanwhile, augmentation devices are used to alter the fluid flow behaviour around VACTs type-H by VG, where the VG is positioned on the blade surface in a configuration of

a pair of VGs along the blade span, as represented in **Fig. 11.** The dimensions, positions, configurations, and types of airfoils determine the success of adding a VG in producing vortex flow with stall delay, increasing lift, and reducing drag. The Darrieus turbine, which drives the VACT, is a lift-driven device. Increasing lift performance is expected to improve turbine efficiency and self-starting capability.



Fig. 12. BRIN vertical-axis ocean current turbine prototype conducted in 2014 (BRIN-documents, 2014)

This section investigates the impact of VG installation on the variation of energy extracted by the VACT, which is assumed to harness hydrokinetic energy from ocean currents. **Fig. 12** illustrates the preparation activities for the field trial of the BRIN vertical-axis ocean current turbine prototype conducted in 2014. In this study, the turbine prototype corresponds to the BRIN marine current turbine previously tested in the Madura Strait, Indonesia. The turbine, equipped with NACA 0021 blades, has a diameter (D) of 3.6 m, a span (s) of 2.18 m, and a chord length (c) of 0.18 m. During field testing, the turbine operated under ocean current velocities (v) ranging from 0.6 to 1.10 m/s, with a cut-in speed of 0.6 m/s and a total power coefficient of 37% by Kasharjanto and Rahuna, (2017). Based on the field test conducted in the Madura Strait, Indonesia, the turbine generated 480 W of power at an ocean current velocity of 1.10 m/s [38].

In this study, it is demonstrated that integrating VGs with the turbine blades improves the flow characteristics around the blades, thereby increasing lift and reducing drag. The enhancement of lift contributes to stall delay and an increase in turbine torque, which ultimately leads to an improvement in the power performance of the vertical-axis marine current turbine. Based on the predicted power enhancement, the addition of square-type VGs results in a 7.5% increase in power output, yielding 518 W. The simulation outcomes demonstrate that positioning the VG at 25% chord on the symmetric NACA 0021 airfoil yields a marked decrease in drag coefficient, accompanied by a significant improvement in lift performance, thereby contributing to stall delay.

4. Conclusion

This study investigated the effect of rectangular VGs on the hydrodynamic performance of the NACA 0021 hydrofoil used in a Vertical Axis Current Turbine (VACT) through CFD simulation using the k–ω SST turbulence model at a Re. 1.917×10^5. The results show that the addition of VGs was able to improve the lift coefficient, reduce drag, delay flow separation, and enhance the overall hydrodynamic efficiency of the hydrofoil, especially at moderate to high angles of attack.

Among the tested configurations, the VG placed at 30%c produced the highest improvement in the lift-to-drag ratio (C_L/C_D), reaching 21.4% compared to the clean hydrofoil. Meanwhile, the VG located at 25%c provided the most significant drag reduction and demonstrated strong capability in delaying stall. Flow visualization also confirmed that the VGs helped maintain flow attachment and reduced wake formation behind the hydrofoil, particularly in near-stall and post-stall conditions.

The improved aerodynamic characteristics directly contributed to better turbine performance. Based on the theoretical prediction using the DMST approach, the integration of VGs on the VACT blade increased the estimated turbine power output from 480 W to 518 W, corresponding to a power enhancement of approximately 7.5%. These findings indicate that VGs are a promising and practical passive flow-control device for improving the performance and self-starting capability of vertical-axis marine current turbines.

Although the present work was limited to steady-state simulations on a single blade, the study provides important initial insights into the influence of VG placement on VACT performance. Future studies are recommended to include full rotating turbine simulations and unsteady flow analysis to better capture dynamic stall behavior and blade interaction effects under realistic operating conditions.

Acknowledgements

The first author specifically expressed his deepest appreciation to the National Research and Innovation Agency of the Republic of Indonesia which funded this project through a scheme called The Education of Degree by Research Doctoral Program, based on the decree of the Deputy for Human Resources in Science and Technology (SDM IPTEK), No. 27/II/HK/2024. This article is one of the targets that must be achieved in implementing the Degree by Research Doctoral Program. This research is also supported by the Research Implementation Program of the Organization Research for Energy and Manufacturing, National Research and Innovation Agency (BRIN), under Research Activity Grant No. 6/III.3/HK/2026.

References

[1] H. D. Taylor. (1947). The elimination of diffuser separation by vortex generators. *Res Dep Rep no r-4012-3, United Aircr Corp East Hartford, Connect*, vol. 103.

[2] X. K. Li, S. Kang, L. P. Dai, and J. D. Jiao. (2015). Effects on airfoil flow field by structure of vortex generators. *K Cheng Je Wu Li Hsueh Pao/Journal Eng Thermophys*, vol. 36, no. 2, pp. 326–329.

[3] S. Georgilidakis. (2022). NASA Puts New Twist on Vortex Generators? https://mentourpilot.com/nasa-puts-new-twist-on-vortex-generators/

[4] Z. Zhao, D. Wang, T. Wang, W. Shen, H. Liu, and M. Chen. (2022). A review: Approaches for aerodynamic performance improvement of lift-type vertical axis wind turbine. *Sustain*

Energy Technol Assessments, vol. 49. doi: 10.1016/J.SETA.2021.101789.

[5] M. Manolesos and S. G. Voutsinas. (2015). Experimental investigation of the flow past passive vortex generators on an airfoil experiencing three-dimensional separation. *J Wind Eng Ind Aerodyn*, vol. 142, pp. 130–148. doi: 10.1016/j.jweia.2015.03.020.

[6] D. Holst, B. Church, F. Wegner, G. Pechlivanoglou, C. N. Nayeri, and C. O. Paschereit. (2019). Experimental Analysis of a NACA 0021 Airfoil under Dynamic Angle of Attack Variation and Low Reynolds Numbers. *J Eng Gas Turbines Power*, vol. 141, no. 3. doi: 10.1115/1.4041146.

[7] A. Saenz-Aguirre, U. Fernandez-Gamiz, E. Zulueta, I. Aramendia, and D. Teso-Fz-Betono. (2022). Flow control based 5 MW wind turbine enhanced energy production for hydrogen generation cost reduction. *Int J Hydrogen Energy*, vol. 47, no. 11, pp. 7049–7061. doi: 10.1016/J.IJHYDENE.2020.01.022.

[8] B. K. Kirke and L. Lazauskas. (2011). Limitations of fixed pitch Darrieus hydrokinetic turbines and the challenge of variable pitch. *Renew Energy*, vol. 36, no. 3, pp. 893–897. doi: 10.1016/J.RENENE.2010.08.027.

[9] M. J. Khan, G. Bhuyan, M. T. Iqbal, and J. E. Quaicoe. (2009). Hydrokinetic energy conversion systems and assessment of horizontal and vertical axis turbines for river and tidal applications: A technology status review. *Appl Energy*, vol. 86, no. 10, pp. 1823–1835. doi: 10.1016/j.apenergy.2009.02.017.

[10] Erwandi *et al.* (2013). Turbin Type Darrieus Poros Vertikal dengan Menggunakan Sudut Serang Pasif yang Fleksibel. IDP000035145.

[11] R. Hantoro, I. K. A. P. Utama, Erwandi, and A. Sulisetyono, "An experimental investigation of passive variable-pitch vertical-axis ocean current turbine," *ITB J Eng Sci*, vol. 43 B, no. 1, pp. 27–40, 2011, doi: 10.5614/itbj.eng.sci.2011.43.1.3.

[12] D. Satrio and I. K. A. P. Utama. (2023). Experimental investigation into the improvement of self-starting capability of vertical-axis tidal current turbine. *Elsevier*. doi: 10.1016/J.EGYR.2021.07.027.

[13] E. M. Suyanto, S. P. Fitri, Erwandi, D. Rahuna, and A. Kasharjanto. (2023). Experimental Study of the Influence Wave Period on the Performance Darrieus Turbine with Modification of the Blade Angle," *IOP Conf Ser Earth Environ Sci*, vol. 1166, no. 1. doi: 10.1088/1755-1315/1166/1/012020.

[14] D. Rahuna, Erwandi, A. Kasharjanto, E. M. Suyanto, and C. S. J. Mintarso. (2023). Experimental Study on Hydrodynamic Aspects of Turbine which Convert Hydrokinetic and Potential Coastal Wave Energy. *IOP Conf Ser Earth Environ Sci*, vol. 1166, no. 1. doi: 10.1088/1755-1315/1166/1/012021.

[15] W. Xu, G. Li, F. Wang, and Y. Li. (2020). High-resolution numerical investigation into the effects of winglet on the aerodynamic performance for a three-dimensional vertical axis wind turbine. *Energy Convers Manag*, vol. 205, no. December 2019. doi: 10.1016/j.enconman.2019.112333.

[16] L. Zhang, X. Li, K. Yang, and D. Xue. (2016). Effects of vortex generators on aerodynamic performance of thick wind turbine airfoils. *J Wind Eng Ind Aerodyn*, vol. 156, pp. 84–92. doi: 10.1016/J.JWEIA.2016.07.013.

[17] W. Miao, Q. Liu, Z. Xu, M. Yue, C. Li, and W. Zhang. (2022). A comprehensive analysis of blade tip for vertical axis wind turbine: Aerodynamics and the tip loss effect. *Energy Convers Manag*, vol. 253, no. September 2021, p. 115140. doi: 10.1016/j.enconman.2021.115140.

[18] S. M. H. Karimian and A. Abdolahifar. (2020). Performance investigation of a new Darrieus Vertical Axis Wind Turbine. *Energy*, vol. 191, p. 116551. doi: 10.1016/j.energy.2019.116551.

[19] D. Satrio *et al.* (2023). Effect of Positioning a Circular Flow Disturbance in front of the Darrieus Turbine. *IOP Conf Ser Earth Environ Sci*, vol. 1166, no. 1. doi: 10.1088/1755-1315/1166/1/012019.

[20] D. Satrio, Suntoyo, and L. I. Ramadhan. (2022). The advantage of flow disturbance for vertical-axis turbine in low current velocity. *Sustain Energy Technol Assessments*, vol. 49. doi: 10.1016/j.seta.2021.101692.

[21] M. B. Salleh, N. M. Kamaruddin, and Z. Mohamed-Kassim. (2021). The effects of a deflector on the self-starting speed and power performance of 2-bladed and 3-bladed Savonius rotors for hydrokinetic application. *Energy Sustain Dev*, vol. 61, pp. 168–180. doi: 10.1016/j.esd.2021.02.005.

[22] D. De Tavernier, C. Ferreira, A. Viré, B. LeBlanc, and S. Bernardy. (2020). Controlling dynamic stall using vortex generators on a wind turbine airfoil," *Renew Energy*, vol. 172, pp. 1194–1211, 2021, doi: 10.1016/j.renene.2021.03.019.

[23] I. K. A. P. Utama *et al.* (2020). Numerical simulation of foil with leading-edge tubercle for vertical-axis tidal-current turbine," *J Mech Eng Sci*, vol. 14, no. 3, pp. 6982–6992. doi: 10.15282/jmes.14.3.2020.02.0547.

[24] D. Rahuna, Erwandi, D. Satrio, and I. K. A. P. Utama. (2024). Opportunities for Utilizing Vortex Generators on Vertical Axis Ocean Current Turbines: A Review. *BIO Web Conf*, vol. 89. doi: 10.1051/bioconf/20248910003.

[25] D. Satrio, Erwandi, and D. Rahuna. (2025). Investigation of enhanced peak lift performance and stall angle delay by attachment of Vortex Generators on blade surfaces of Vertical Axis Ocean Current Turbine. *Ocean Eng*, vol. 326, p. 120762. doi: 10.1016/J.OCEANENG.2025.120762.

[26] L. Galera, P. Martinez-Filgueira, U. Fernández-Gámiz, E. Zulueta, J. M. Lopez, and J. M. Blanco. (2019). A triangular vortex generator modeling on a DU97-W-300 airfoil by a source term model," *Proc Inst Mech Eng Part A J Power Energy*, vol. 233, no. 5, pp. 635–645. doi: 10.1177/0957650919850449.

[27] H. Müller-Vahl, G. Pechlivanoglou, C. Nayeri, and C. Paschereit, *Vortex Generators for Wind Turbine Blades: A Combined Wind Tunnel and Wind Turbine Parametric Study*, vol. 6. 2012. doi: 10.1115/GT2012-69197.

[28] D. Baldacchino, C. Ferreira, D. De Tavernier, W. A. Timmer, and G. J. W. van Bussel. (2018). Experimental parameter study for passive vortex generators on a 30% thick airfoil: Experimental parametric vortex generator study. *Wind Energy*, vol. 21, no. 9, pp. 745–765. doi: 10.1002/WE.2191.

[29] H. Wang, B. Zhang, Q. Qiu, and X. Xu. (2017). Flow control on the NREL S809 wind turbine airfoil using vortex generators," *Energy*, vol. 118, pp. 1210–1221. doi: 10.1016/j.energy.2016.11.003.

[30] B. Wei, Y. Gao, and S. Hu. (2023). Experimental Study on Multiobjective Flow Control of Dynamic Stalls Using a Vortex Generatorle. *J Aerosp Eng*, vol. 36, no. 6. doi: https://doi.org/10.1061/JAEEEZ.ASENG-4989.

[31] F. M. Kale, N. Yilmaz, K. F. Sokmen, and W. Shi. (2025). Experimental and numerical investigations of hydrodynamic

performance for horizontal-axis hydrokinetic turbines. *Brodogradnja* vol. 76, no. 3.

[32] W. Shi, M. Atlar, R. Norman, B. Aktas, and S. Turkmen. (2016). Numerical optimization and experimental validation for a tidal turbine blade with leading-edge tubercles. *Renew Energy*, vol. 96, pp. 42–55. doi: 10.1016/J.RENENE.2016.04.064.

[33] M. I. Zafar, M. M. Choudhari, P. Paredes, and H. Xiao. (2021). Recurrent neural network for end-to-end modeling of laminar-turbulent transition. doi: 10.1017/dce.2021.11.

[34] Y. Yan, E. Avital, J. Williams, and J. Cui. (2019). CFD analysis for the performance of micro-vortex generator on aerofoil and vertical axis turbine. *J Renew Sustain Energy*, vol. 11, no. 4. doi: 10.1063/1.5110422.

[35] ITTC. (2017). The Specialist Committee on CFD and EFD Combined Methods Final Report and Recommendations to the 29th ITTC. *ITTC – Recomm Proced Guidel Guidel Spec Comm CFD EFD Comb Methods*, pp. 1–8. https://ittc.info/media/9098/sc-combined-cfd-efd-methods.pdf

[34] J. C. Lin. (2002). Review of research on low-profile vortex generators to control boundary-layer separation. *Pergamon*. doi: 10.1016/S0376-0421(02)00010-6.

[35] N. Troldborg, F. Zahle, and N. N. Sørensen. (2015). Simulation of a MW rotor equipped with vortex generators using CFD and an actuator shape model. *53rd AIAA Aerosp Sci Meet*, no. January, pp. 1–10. doi: 10.2514/6.2015-1035.

[36] A. Kasharjanto, D. Rahuna, and D. Rina. (2017). Kajian Pemanfaatan Energi Arus Laut Di Indonesia - Study on the Implementation Of Marine Current Energy In Indonesia. *Jurnal Ilmiah Teknologi Maritim*, vol. 11, no. 2, pp. 75–84. (in Indonesia language).